1-1-2024

Cellular structure mediated dislocation regulation in additively manufactured refractory high entropy alloy

Changxi Liu

Lechun Xie

Lai-Chang Zhang
Edith Cowan University

Liqiang Wang

10.1080/21663831.2024.2341937
Liu, C., Xie, L., Zhang, L. C., & Wang. L. (2024). Cellular structure mediated dislocation regulation in additively manufactured refractory high entropy alloy. Materials Research Letters, 12(6), 425-432. https://doi.org/10.1080/21663831.2024.2341937

Materials Research Letters

ISSN: (Print) (Online) Journal homepage: www.tandfonline.com/journals/tmrl20

Cellular structure mediated dislocation regulation in additively manufactured refractory high entropy alloy

Changxi Liu, Lechun Xie, Lai-Chang Zhang & Liqiang Wang

To cite this article: Changxi Liu, Lechun Xie, Lai-Chang Zhang & Liqiang Wang (2024) Cellular structure mediated dislocation regulation in additively manufactured refractory high entropy alloy, Materials Research Letters, 12:6, 425-432, DOI: 10.1080/21663831.2024.2341937

To link to this article: https://doi.org/10.1080/21663831.2024.2341937

MATER. RES. LETT.
2024, VOL. 12, NO. 6, 425–432
https://doi.org/10.1080/21663831.2024.2341937

Cellular structure mediated dislocation regulation in additively manufactured refractory high entropy alloy

Changxi Liu[a], Lechun Xie[b,c], Lai-Chang Zhang[d] and Liqiang Wang[a]

[a]State Key Laboratory of Metal Matrix Composites, School of Material Science and Engineering, Shanghai Jiao Tong University, Shanghai, People's Republic of China; [b]Hubei Key Laboratory of Advanced Technology for Automotive Components, Wuhan University of Technology, Wuhan, People's Republic of China; [c]Hubei Collaborative Innovation Center for Automotive Components Technology, Wuhan, People's Republic of China; [d]Centre for Advanced Materials and Manufacturing, School of Engineering, Edith Cowan University, Perth, Australia

ABSTRACT

A Ti1.5Nb1Ta0.5Zr1Mo0.5 (TNTZM) refractory high entropy alloy (HEA) with a cellular structure was successfully fabricated by laser powder bed fusion (L-PBF). Compression testing and cyclic deformation testing results revealed that, in the cellular structure, the cell walls could store dislocations. Furthermore, the local chemical order (LCO) plays a crucial role in controlling dislocations within the cell wall region. The LCO not only facilitates dislocation slip but also generates additional lattice distortion upon stress-induced LCO destruction to enable dislocation pinning. This work offers novel insights into the microstructure of additively manufactured refractory HEAs and uncovers a distinct dislocation regulation mechanism.

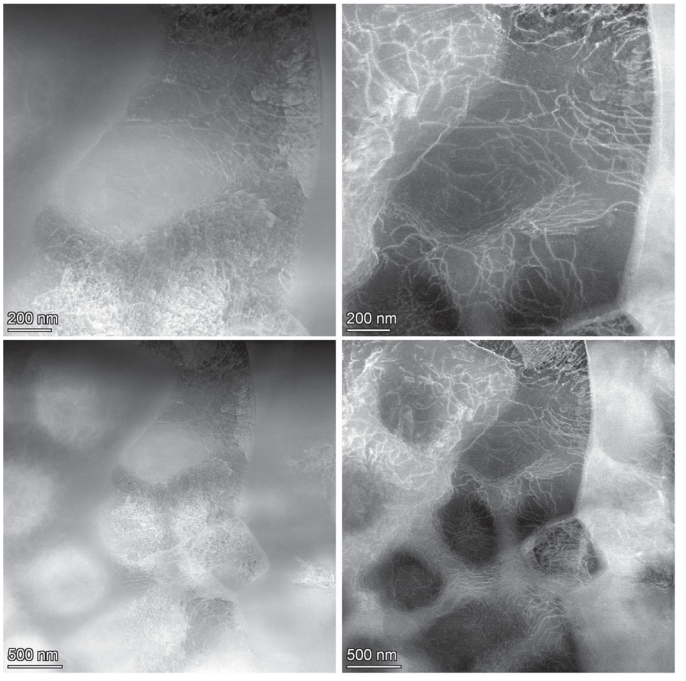

ARTICLE HISTORY
Received 31 January 2024

Since Yeh discovered high entropy alloys (HEAs) in 2004 [1], HEAs have demonstrated a wide range of alloy design possibilities, together with exceptional mechanical and functional properties [2–11]. Recently, there has been significant research interest in a new type of HEAs called refractory HEAs [12], which typically comprise refractory elements such as Ti, Nb, Ta, Zr, and so on and exhibit a body-centered cubic (BCC) crystal structure.

CONTACT Liqiang Wang wang_liqiang@sjtu.edu.cn State Key Laboratory of Metal Matrix Composites, School of Material Science and Engineering, Shanghai Jiao Tong University, No. 800 Dongchuan Road, Shanghai, 200240, China; Lai-Chang Zhang lczhangimr@gmail.com Centre for Advanced Materials and Manufacturing, School of Engineering, Edith Cowan University, 270 Joondalup Drive, Joondalup, Perth, 6027, Australia

Supplemental data for this article can be accessed online at https://doi.org/10.1080/21663831.2024.2340637.

Compared with previous HEAs, refractory HEAs may have the potential to exhibit superior performance in high-temperature applications [13] and in the medical implant field [14,15].

Additive manufacturing is also a significant and emerging manufacturing technology owing to its rapid construction capabilities and exceptional design freedom [16–22]. For refractory HEAs, the rapid and comprehensive processing capabilities offered by AM technology compared to conventional arc melting methods are particularly attractive. However, the preparation of refractory HEAs using AM poses significant challenges [23]. This is attributed to the elevated and significantly varying melting points of the constituent elements of refractory HEAs, which makes the fabrication process prone to introducing defects that can ultimately lead to failure. With the recent rapid advancement of AM technology, Dobbelstein [24] successfully prepared TiZrNbHfTa refractory HEA using laser metal deposition, and subsequently more AM-fabricated refractory HEAs were reported [25–27]. Furthermore, AM-fabricated metals usually exhibit distinct microstructures compared to conventionally-processed metals. Indeed, cellular structures are an unusual type of microstructure introduced by AM. This structure is composed of cell walls and cell interiors and has been observed in steels [28,29], copper alloys [30], and aluminum alloys [31]. The cellular structure present within grains can significantly affect the mechanical properties of the material [30,32]. However, to date, there are no studies reporting on the presence of cellular structures in AM-fabricated refractory HEAs. Therefore, in order to reveal the microstructure of AM-fabricated refractory HEAs, further study on the cellular structure in refractory HEAs is needed.

Based on our previous research [33], it has been demonstrated that the mechanical properties and deformation mechanism of TNTZM are closely associated with its cellular structure. Here, a Ti1.5Nb1Ta0.5Zr1Mo 0.5 (TNTZM) refractory HEA with cellular structure was successfully fabricated using laser powder bed fusion (L-PBF) technology, aiming to further investigate the interaction between the cellular structure and dislocation. Furthermore, compression tests and cyclic deformation processing (CP) experiments revealed that the cellular structure has the ability to influence dislocation slip within grains. In addition, some local chemical ordering (LCO) containing Ti atoms are present within the cell wall, which makes the cell wall able to restrict dislocations movement. This work aims to improve the AM-fabricated refractory HEA systems and to propose a novel microscopic mechanism for regulating dislocations.

Mechanical alloying of Ti, Ta, Nb, Zr, and Mo spherical powders (99% purity) in the particle size range from 40 μm to 90 μm using a Pulverizette-4 planetary ball mill for 40 h, as illustrated in Figure S1. To determine the optimal process window for fabricating TNTZM, a total of 72 different printing parameters (including laser power and scan speed), as shown in Figure S2, were tested using an M2 Multilaser machine (Concept Laser, Germany). The experimental results indicated that a laser power of 240 W and a scan speed of 1700mm/s resulted in the highest density of 99.5% along with a uniform distribution of elements in the fabricated TNTZM. AM-fabricated TNTZM was cut by electrical discharge machining, and its surface was subsequently ground using metallographic SiC papers ranging from 100 to 2000 grits. This was followed by polishing with diamond suspensions of 3 and 1 μm. Figure 1(a) shows the electron backscatter diffraction (EBSD) analysis results, indicating that the AM-fabricated TNTZM is a single-phase refractory HEAs with a BCC structure. Additionally, the Figure S3 shows that there is no significant grain anisotropy observed across different building directions. Furthermore, the polar plots indicate the maximum intensity value in the plot is 1.68. As seen in Figure 1(a), it is suggested that there is no evident texture in AM-fabricated TNTZM. Specifically, the average grain size was determined to be 8μm (Figure S4), which is significantly larger than the size of cells. This observation suggests that the cells represent submicroscopic structures within the grain. Furthermore, the absence of discernible cellular structures in the EBSD results suggests that EBSD may not have the capability to identify cells. This is because adjacent cells exhibit the same grain orientation. Figure 1(b) illustrates the morphology of the cellular structure in backscattered electron (BSE) mode, where the dimensions typically fall within the range of 260-370 nm and the bright cell interiors and dark cell walls are clearly visible. Furthermore, it is observed that this cellular structure consisting of cell interior and cell walls is widespread in AM-fabricated TNTZM.

In addition, compositional maps in transmission electron microscopy (TEM) reveal the segregation of Ta and Nb, as well as the aggregation of Ti, along the cell walls of the solidified cellular structures in Figure 2(a). It is evident that the cell walls are approximately 50 nm wide and surround the cell interior. The selected area electron diffraction (SAED) pattern at the interface between the cell wall and cell interior displays a typical pattern of a BCC structure, in the absence of any other patterns. furthermore, AM-fabricated TNTZM was identified by X-ray diffraction (XRD) using a commercial D8 ADVANCE Da Vinci machine. The XRD results indicate the presence of two types of BCC peaks. One set of peaks corresponds to unmelted Mo powder (Figure S5), while the other set corresponds to the BCC structure of

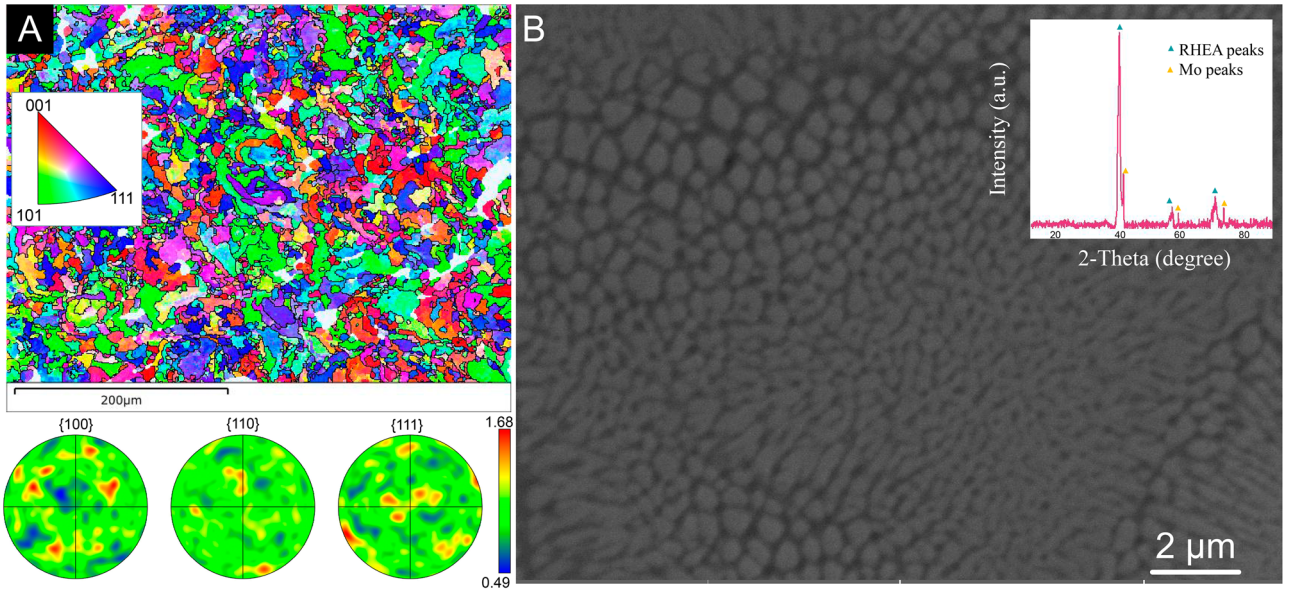

Figure 1. (A) EBSD image of the AM-fabricated TNTZM. The diagrams in the bottom are the corresponding polar figures. (B) BSE SEM image of the AM-fabricated TNTZM, where the black area is the cell wall and the grey area is the cell interior. The inserts are the XRD pattern of the AM-fabricated TNTZM.

TNTZM (Figure 1(b)). Furthermore, previous researches [21,34] indicates that AM utilizing mechanical alloying powders may result in the presence of unmelted powder within the matrix. Indeed, the SAED results and the XRD results assert that both the cell walls and cell interior exhibit identical crystal structure. This cellular structure in AM-fabricated TNTZM is different from that of aluminum alloys [31], which typically consists of a matrix wrapped by a second phase. Figure 2(b) displays a scanning transmission electron microscope (STEM) image in high-angle annular dark-field (HAADF) mode, which enhances sensitivity to the atomic number and enables accurate visualization of the cellular structure morphology. Figure 2(c) displays a dark-field (DF) image used to assess the dislocation distribution in the same region as the HADDF mode. The DF image indicates that dislocations in the as-built TNTZM are randomly dispersed inside the cells and within the cell walls, and they are minimally affected by the cell walls. Based on these TEM results, it can be concluded that the cellular structure in AM-fabricated TNTZM is formed by elemental segregation rather than dislocations [35] or the presence of a second phase [36], which aligns with previous research [33,37].

In compression tests, only dislocation slip was observed as the dominant deformation mode in TNTZM, and no phase transformation or twinning was detected. When the applied strain increases to 10%, it is observed that dislocations start to develop and move in response to external shear stress. In addition to the minimal change in cell shape after deformation, surprisingly, a majority of dislocations are stored within the cell walls, and other dislocations accumulate next to the cell walls, as shown in Figure 2(d,e). Furthermore, when the deformation increases to 18%, dislocation channels are formed within the cell walls, and the tangled dislocations are observed sliding out from the channels (Figure 2(f,g)). This confirms that the presence of the cell wall significantly affects the generation and movement of dislocations.

To further investigate the influence of cellular structure on dislocation regulation, cyclic deformation processing (CP) was applied to TNTZM (CP-TNTZM) within the microplastic region to induce slight residual stress. Figure 3(a,b) presents the cyclic stress–strain diagrams of the as-built TNTZM, depicting the stages of deformation at 2.5% strain, recovery to 0% strain, and subsequent deformation to 2.5% strain. Remarkably, this cyclic deformation was repeated for a total of 100 cycles. Figure 3(c) shows the individual cellular structure of the as-built TNTZNM after CP in HADDF mode, where the darker regions represent the Ti-rich cell walls, and the lighter regions are the cell interiors. Exactly as illustrated in Figure 3(d), the dark-field image clearly reveals that the dislocations in TNTZM are noticeably influenced by the cellular structure in CP-TNTZM. Dislocations are also stored within the cell wall or accumulated near to the cell walls, similar to the deformed TNTZM as shown in Figure 2(d,e). Furthermore, this observation suggests that, during cyclic deformation, dislocations tend to become pinned to each other. Based on the XRD analysis (Figure S6), the dislocation density of TNTZM was found to increase from 2.22×10^{15}

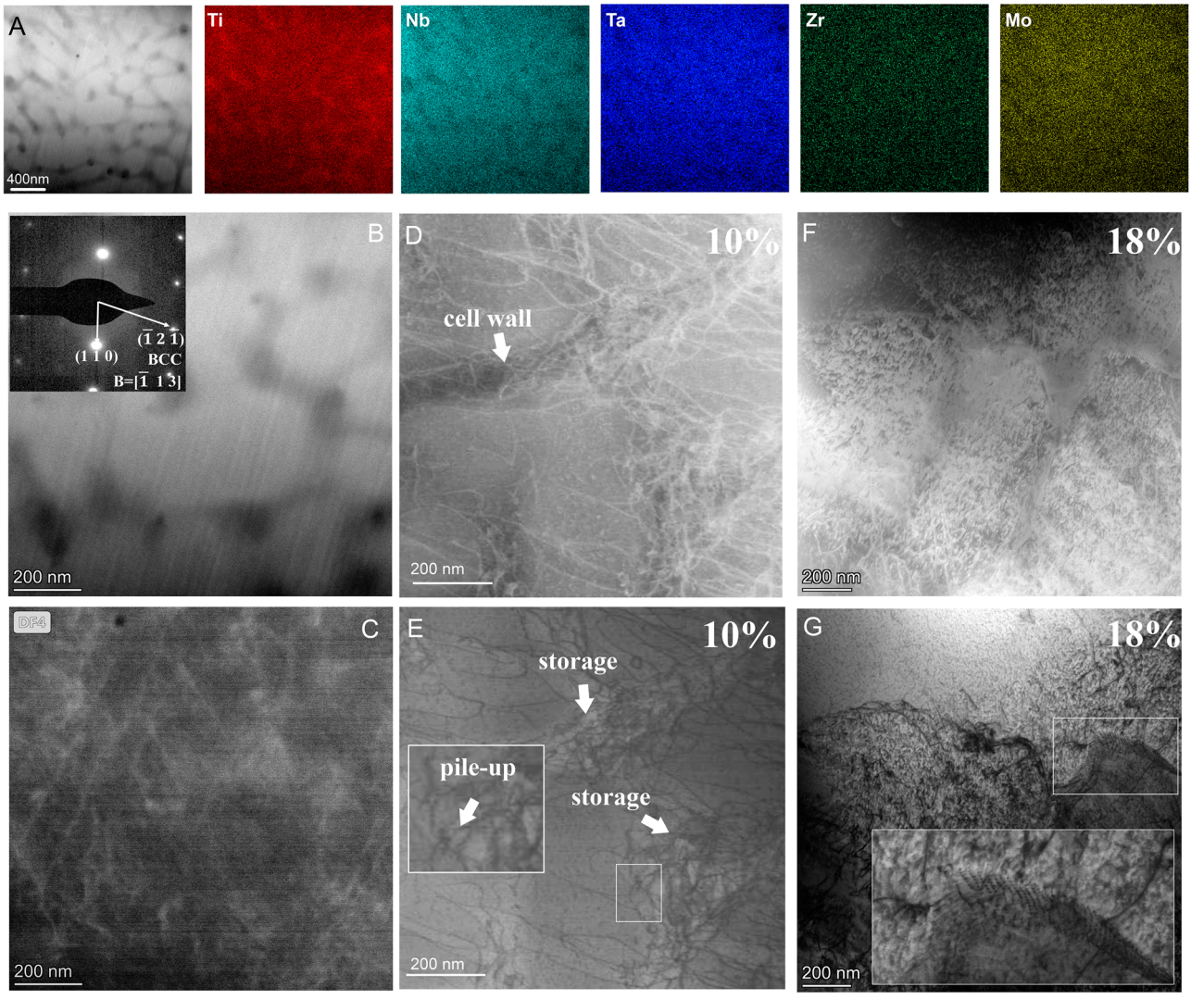

Figure 2. (A) The compositional mappings of the cellular structure in TNTZM. (B) The morphology of cellular structure in HADDF mode. (C) The dislocation distribution in cellular structure in DF mode. (D) The morphology of the cellular structure after undergoing a 10% deformation in HADDF mode. (E) The distribution of dislocations within the cellular structure after undergoing a 10% deformation in DF mode. (F) The morphology of the cellular structure after undergoing an 18% deformation in HADDF mode. (G) The morphology of the dislocation channel after undergoing an 18% deformation in DF mode.

m^{-2} to 4.31×10^{15} m^{-2} after cycling. This finding further supports the previous conclusion that the cellular structure in AM-fabricated TNTZM has a significant regulatory effect on dislocation motions. The cellular structure exhibits a flexible capability to respond to dislocation motion, not only limited to large plastic deformations (compression testing) but also to deformation within the microplastic regions.

Furthermore, dislocation channels in CP-TNTZM are observed to be located in the cell walls, as shown in Figure 3(e,f), which is consistent with the dislocation channels observed in TNTZM after the compression testing in Figure 3(h). Previous studies [38] have demonstrated that dislocations located in the dislocation channels encounter challenges when attempting to cross-slip out, leading to rapid saturation of dislocation accumulation within the dislocation channels. The generation of dislocation channels in the cell walls facilitates the accumulation of dislocations. This is why dislocations are more easily stored in cell walls. Furthermore, the presence of dislocation channels within the cell walls provides an easier pathway for dislocation slip, resulting in widespread dislocation propagation within the cell walls in TNTZM during the initial stages of compression tests and cyclic deformation. Moreover, the diffusion of dislocation channels creates opportunities for multiple dislocations to interact. Figure 3(h) visually illustrates this phenomenon, showing the presence of dislocation tangles commonly observed in CP-TNTZM. Indeed, it is the numerous intersections formed by dislocation channels

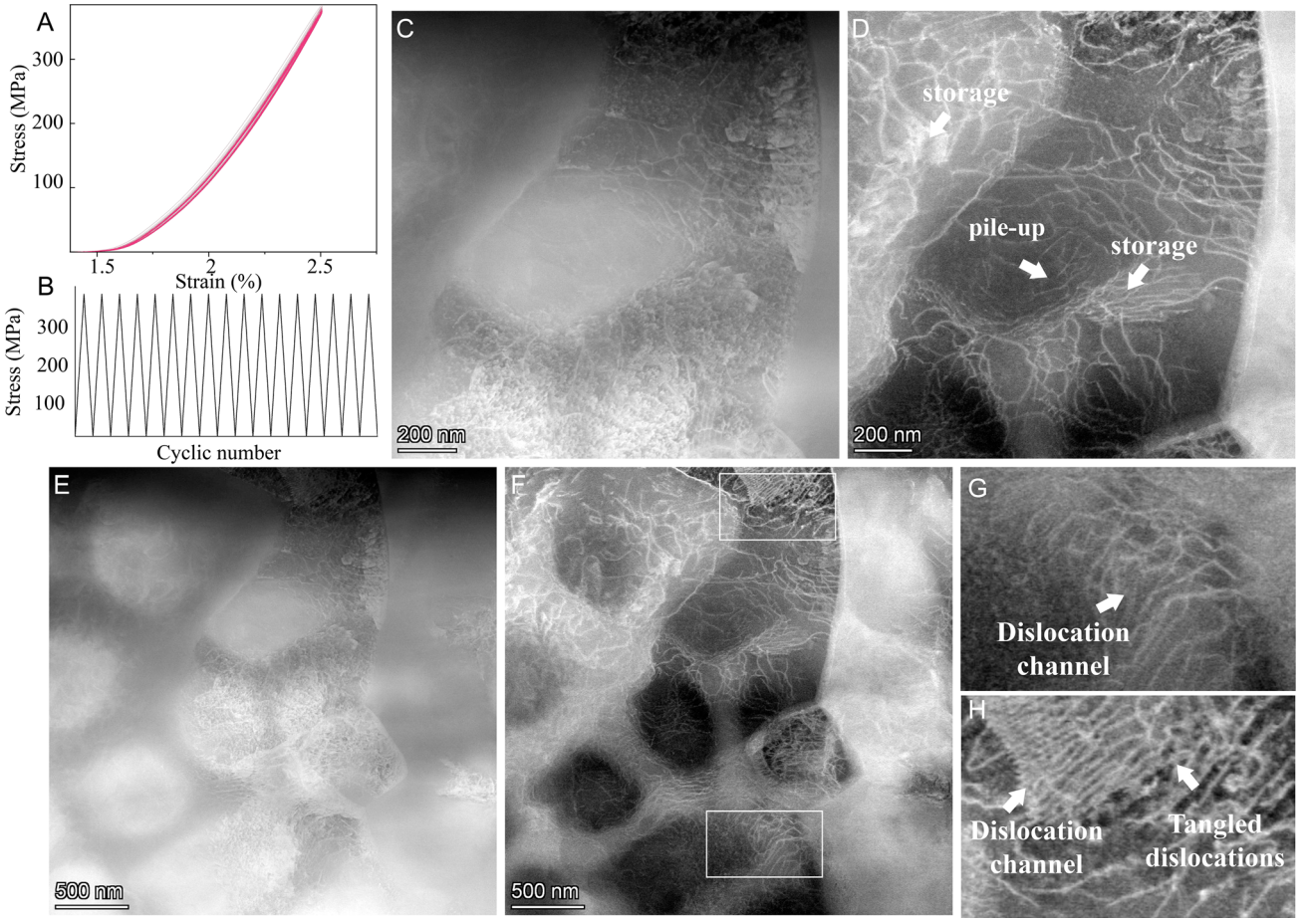

Figure 3. (A-B) Stress–strain responses during CP. (C) The morphology of cellular structure after undergoing CP in HADDF mode. (D) Dislocation storage and pile-up in cell wall. (E) The HADDF model corresponds to (F). (F) The morphology of the dislocation channel after undergoing CP. (G) dislocation channel in cell wall. (H) Entanglement of dislocation channels and dislocation.

that result in dislocation entanglement. This entanglement leads to mutual obstruction of dislocations and an increasing dislocation density in the cell wall region. As the dislocation density increases in the cell wall region, the movement of dislocations within the cell interior is significantly affected. In particular, in the initial stages of compression tests and cyclic deformation, dislocations located inside the cells are observed to pile up near the cell wall regions, as shown in Figure 2(e) and Figure 3(d). This phenomenon is attributed to the effective storage of dislocations within the cell walls, which creates an additional stress field and impedes dislocations inside the cells until higher external shear stresses are encountered.

Furthermore, Figure 4(a) displays a HAADF image of the atomic structure within the cell wall region (Figure S7), which was obtained using aberration-corrected STEM under the [100] zone axis. The fast Fourier transform (FFT) pattern of the AM-fabricated TNTZM exhibits the standard BCC structure discs. The inverse FFT (IFFT) process of the 001 planes in the FFT mode identifies the LCO regions as shown in Figure 4(b). These regions indicate the presence of additional or increased chemical order in the material (Figure 4(c,d)). Considering the atom column in HADDF mode, the image contrast shows high sensitivity to atomic number. Observation of the dark regions of the LCO region suggests that it is mainly composed of lighter elements (Ti), consistent with previous compositional mapping results showing that Ti atoms are enriched in the cell wall region. Figure 4(f) illustrates a schematic diagram of the distribution of LCO in the BCC lattice and its projection along the [100] yellow arrow direction. This description provides further insight into the construction of LCO. According to previous studies [38], it is generally believed that LCO is only partially developed within a limited spatial extent; for instance, it may contain only a few atomic layers in the thickness direction, even though it is already long-range in another dimension. On the low-end side, LCO exhibits chemical short-range ordering, while at the other extreme it can be considered as an early stage of nanoprecipitates. Furthermore, the diffraction signal from LCO, including chemical short-range order, is often

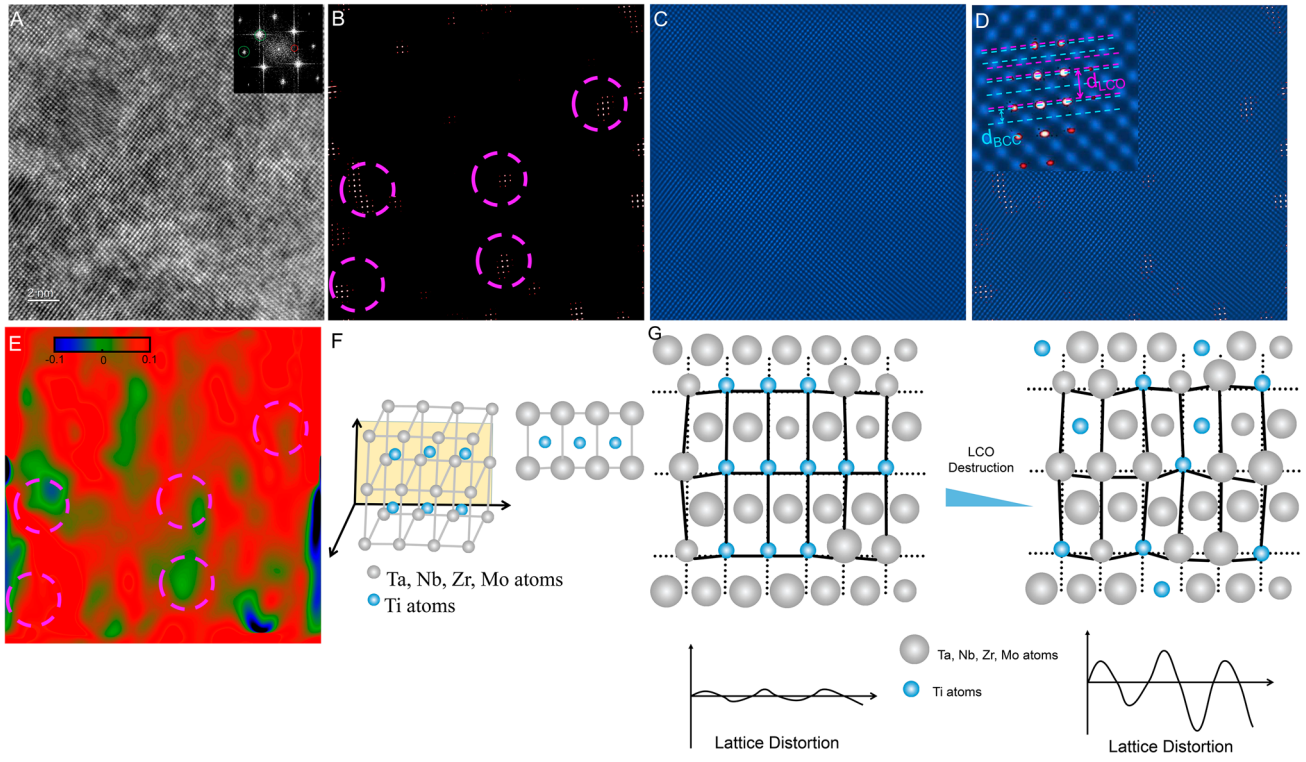

Figure 4. (A) The atomic structure morphology of the cell wall in HADDF mode. The inset is the corresponding FFT pattern, where the red solid circles indicate the LCOs region and the green solid circles indicate the Bragg spots of the BCC matrix. (B) The IFFT process of the red solid circles in (A), and several LCOs are marked by purple circles. (C) The IFFT process of the green solid circles in (A) shows the BCC lattice. (D) The image superimposes the corresponding images of the LCO and BCC IFFT image. (E) The atomic-strain mappings of the cell wall (F) The schematic diagram of LCO. (G) The schematic illustrations of the effect of LCO destruction on the lattice distortion.

weak and diffuse and may exhibit additional features such as fringes.

HEAs usually demonstrate strong lattice distortion caused by variations in atomic radius among multiple constituent elements. However, incorporating LCO into the nanoscale structure of HEAs, especially refractory HEAs, can effectively mitigate lattice distortion. Figure 4(e) illustrates the mapping of the corresponding atomic strains using geometrical phase analysis (GPA), indicating that the lattice distortion in the LCO region of TNTZM is relatively lower than those in other regions. This observation is consistent with previous findings [38]. This phenomenon can be attributed to the regular arrangement of Ti elements within the LCO region, as depicted in Figure 4(f). This ordered arrangement contrasts with the disordered distribution of elements in the HEA matrix, significantly reducing lattice distortion. Due to the widespread presence of LCO in the cell wall region, dislocation channels tend to proliferate, reducing lattice distortion and promoting the softening of the slip planes. Therefore, under conditions with additional shear stress, such as during cyclic deformation and early stages of deformation, dislocation channels are observed to proliferate in the cell wall. As the LCO region suffers damage, the lattice distortion within this region gradually increases, approaching the strong lattice distortion present in conventional refractory HEAs. This impedes dislocation motion, and the effects caused by lattice distortion start to catch up with the softening of the slip plane due to the destruction of LCOs. Consequently, the hindrance of dislocation motion caused by lattice distortion gradually catches up with the softening of the slip plane caused by the residual LCO. Figure 2(g) and Figure 3(h) demonstrate the dislocation tangles at dislocation channel intersections, which are caused by multiple dislocations sliding within the cell walls, triggering the destruction of LCO. Additionally, the self-assembly of dislocations in the cellular structure is achieved through the accumulation of dislocations caused by the initial softening of LCO in the cell wall and the pinning of dislocations caused by the destruction of LCOs. A large number of dislocations within the cell walls can also lead to self-hardening of the cell walls, which significantly affects the movement of dislocations within the cells.

In summary, a TNTZM refractory HEA with cellular structure was successfully fabricated using L-PBF. The cellular structure significantly modulates the distribution of dislocations in the external shear environment.

The cell walls store dislocations to self-harden, and then impede dislocation slip inside the cells. In addition, LCO facilitates the formation of numerous dislocation channels within the cell walls, and these channels promote the proliferation of dislocations in the initial stage. Moreover, when the LCO undergoes destruction, these dislocations are also anchored in the cell wall, leading to the self-assembly of dislocations. This work provides new insights into the heterogeneous microstructure of AM-fabricated refractory HEAs.

CRediT authorship contribution statement

Changxi Liu: Conceptualization, Methodology, Investigation, Writing — original draft, Writing — review & editing. **Lechun Xie:** Writing — review & editing. **Lai-Chang Zhang:** Conceptualization, Methodology, Investigation, Writing — original draft, Writing — review & editing, Supervision. **Liqiang Wang:** Conceptualization, Methodology, Investigation, Writing — review & editing, Supervision, Funding.

Data availability

The data that support the findings of this study are available from the corresponding author upon request.

Acknowledgements

The authors acknowledge the financial supports from National Natural Science Foundation of China under (Grant Nos. 52274387).

Disclosure statement

No potential conflict of interest was reported by the author(s).

Impact statment

This work presents a study on the effect of cellular structure on the distribution of dislocations in additively manufactured refractory HEAs.

Funding

This work was supported by National Natural Science Foundation of China [grant number: 52274387].

References

[1] Yeh JW, Chen SK, Lin SJ, et al. Nanostructured high-entropy alloys with multiple principal elements: Novel alloy design concepts and outcomes. Adv Eng Mater. 2004;6:299–303.
[2] Lei Z, Liu X, Wu Y, et al. Enhanced strength and ductility in a high-entropy alloy via ordered oxygen complexes. Nature. 2018;563:546–550.
[3] Bu Y, Wu Y, Lei Z, et al. Local chemical fluctuation mediated ductility in body-centered-cubic high-entropy alloys. Mater Today. 2021;46:28–34.
[4] Yang Y, Chen T, Tan L, et al. Bifunctional nanoprecipitates strengthen and ductilize a medium-entropy alloy. Nature. 2021;595:245–249.
[5] Shi P, Li R, Li Y, et al. Hierarchical crack buffering triples ductility in eutectic herringbone high-entropy alloys. Science (80-). 2021;373:912–918.
[6] Shi P, Zhong Y, Li Y, et al. Multistage work hardening assisted by multi-type twinning in ultrafine-grained heterostructural eutectic high-entropy alloys. Mater Today. 2020;41:62–71.
[7] Shen J, Lopes JG, Zeng Z, et al. Deformation behavior and strengthening effects of an eutectic AlCoCrFeNi2.1 high entropy alloy probed by in-situ synchrotron X-ray diffraction and post-mortem EBSD. Mater Sci Eng A. 2023;872:144946.
[8] Shen J, Zhang W, Lopes JG, et al. Evolution of microstructure and deformation mechanisms in a metastable Fe42Mn28Co10Cr15Si5 high entropy alloy: A combined in-situ synchrotron X-ray diffraction and EBSD analysis. Mater Des. 2024;238:112662.
[9] Jiang D, Xie L, Wang L. Current application status of multi-scale simulation and machine learning in research on high-entropy alloys. J Mater Res Technol. 2023;26:1341–1374.
[10] Liu C, Wang Y, Zhang Y, et al. Additively Manufactured High-Entropy Alloys: Exceptional Mechanical Properties and Advanced Fabrication. Acta Metall Sin (English Lett) [Internet]. 2024;37:3–16. doi:10.1007/s40195-023-01644-2
[11] Shen J, Choi YT, Yang J, et al. Fabrication of spatially-variable heterostructured CoCrFeMnNi high entropy alloy by laser processing. Mater Sci Eng A. 2024;896:146272.
[12] Senkov ON, Wilks GB, Scott JM, et al. Mechanical properties of Nb25Mo25Ta 25W25 and V20Nb20Mo 20Ta20W20 refractory high entropy alloys. Intermetallics. 2011;19:698–706.
[13] Lee C, Kim G, Chou Y, et al. Temperature dependence of elastic and plastic deformation behavior of a refractory high-entropy alloy. Sci Adv. 2020;6:eaaz4748.
[14] Liu C, Yang C, Liu J, et al. Medical high-entropy alloy: Outstanding mechanical properties and superb biological compatibility. Front Bioeng Biotechnol. 2022;10:1–15.
[15] Feng J, Tang Y, Liu J, et al. Bio-high entropy alloys: Progress, challenges, and opportunities. Front Bioeng Biotechnol. 2022;10:1–26.
[16] Huang SH, Liu P, Mokasdar A, et al. Additive manufacturing and its societal impact: A literature review. Int J Adv Manuf Technol. 2013;67:1191–1203.
[17] Gu D, Shi X, Poprawe R, et al. Material-structure-performance integrated laser-metal additive manufacturing. Science (80-). 2021;372:eabg1487.
[18] Summary R. Multiprocess 3D printing for increasing component functionality. 2016;353:aaf2093.
[19] Chen LY, Liang SX, Liu Y, et al. Additive manufacturing of metallic lattice structures: Unconstrained design, accurate fabrication, fascinated performances, and challenges. Mater Sci Eng R Reports. 2021;146:100648.

[20] Zhang Y, Wei D, Chen Y, et al. Non-negligible role of gradient porous structure in superelasticity deterioration and improvement of NiTi shape memory alloys. J Mater Sci Technol. 2024;186:48–63.
[21] Zhang LC, Wang J. Stabilizing 3D-printed metal alloys A design strategy overcomes the strength-ductility trade-off in alloy manufacturing. Science (80-). 2024;383:586–587.
[22] Ma HY, Wang JC, Qin P, et al. Advances in additively manufactured titanium alloys by powder bed fusion and directed energy deposition: Microstructure, defects, and mechanical behavior. J Mater Sci Technol. 2024;183:32–62.
[23] Dobbelstein H, Gurevich EL, George EP, et al. Laser metal deposition of compositionally graded TiZrNbTa refractory high-entropy alloys using elemental powder blends. Addit Manuf. 2019;25:252–262.
[24] Dobbelstein H, Gurevich EL, George EP, et al. Laser metal deposition of a refractory TiZrNbHfTa high-entropy alloy. Addit Manuf. 2018;24:386–390.
[25] Gou S, Gao M, Shi Y, et al. Additive manufacturing of ductile refractory high-entropy alloys via phase engineering. Acta Mater. 2023;248:118781.
[26] Zhang H, Zhao Y, Cai J, et al. High-strength NbMoTaX refractory high-entropy alloy with low stacking fault energy eutectic phase via laser additive manufacturing. Mater Des. 2021;201:109462.
[27] Feng J, Wei D, Zhang P, et al. Preparation of TiNbTaZrMo high-entropy alloy with tunable Young's modulus by selective laser melting. J Manuf Process [Internet]. 2023;85:160–165. doi:10.1016/j.jmapro.2022.11.046
[28] Wang YM, Voisin T, McKeown JT, et al. Additively manufactured hierarchical stainless steels with high strength and ductility. Nat Mater. 2018;17:63–70.
[29] Li Z, He B, Guo Q. Strengthening and hardening mechanisms of additively manufactured stainless steels: The role of cell sizes. Scr Mater. 2020;177:17–21.
[30] Li Z, Cui Y, Yan W, et al. Enhanced strengthening and hardening via self-stabilized dislocation network in additively manufactured metals. Mater Today [Internet]. 2021;50:79–88. Available from: doi:10.1016/j.mattod.2021.06.002
[31] Yan C, Hao L, Hussein A, et al. Microstructure and mechanical properties of aluminium alloy cellular lattice structures manufactured by direct metal laser sintering. Mater Sci Eng A [Internet]. 2015;628:238–246. doi:10.1016/j.msea.2015.01.063
[32] Pan Q, Zhang L, Feng R, et al. Gradient cell–structured high-entropy alloy with exceptional strength and ductility. Science (80-). 2021;374:984–989.
[33] Liu C, Wang Y, Zhang Y, et al. Deformation mechanisms of additively manufactured TiNbTaZrMo refractory high-entropy alloy: The role of cellular structure. Int J Plast [Internet]. 2024;173:103884. doi:10.1016/j.ijplas.2024.103884
[34] Wang J, Liu Y, Rabadia CD, et al. Microstructural homogeneity and mechanical behavior of a selective laser melted Ti-35Nb alloy produced from an elemental powder mixture. J Mater Sci Technol [Internet]. 2021;61:221–233. doi:10.1016/j.jmst.2020.05.052
[35] Levine LE, Larson BC, Yang W, et al. X-ray microbeam measurements of individual dislocation cell elastic strains in deformed single-crystal copper. Nat Mater. 2006;5:619–622.
[36] Prashanth KG, Eckert J. Formation of metastable cellular microstructures in selective laser melted alloys. J Alloys Compd. 2017;707:27–34.
[37] Bang X, Wenpeng J, Huiping T, et al. Microstructure and mechanical properties of a newly developed WTaRe refractory alloy by selective electron beam melting. Addit Manuf. 2022;54:102728.
[38] Wang L, Ding J, Chen S, et al. Tailoring planar slip to achieve pure metal-like ductility in body-centred-cubic multi-principal element alloys. Nat Mater. 2023;22:950–957.